CHEMISTRY OF MATERIALS

pubs.acs.org/cm

Article

Metastability and Photoelectrochemical Properties of Cu_2SnO_3 and $Cu_{2-x}Li_xTiO_3$: Two Cu(I)-Based Oxides with Delafossite Structures

Shaun O'Donnell, Reinhard K. Kremer, and Paul A. Maggard*

Cite This: *Chem. Mater.* 2023, 35, 1404−1416

Read Online

ACCESS | Metrics & More | Article Recommendations | Supporting Information

ABSTRACT: Metastable, *p*-type Cu(I)-based semiconductors were synthesized using cation-exchange reactions between delafossite-type layered precursors and CuCl flux, yielding Cu_2SnO_3 (**I**) and $Cu_{2-x}Li_xTiO_3$ (**II**, $x_{min} \sim 0.4$). These represent the first reported crystalline semiconductors found in the Cu−Sn−O or Cu−Ti−O chemical systems (and not currently predicted within any materials databases), with their kinetic stabilization requiring a relatively low reaction temperature of ∼475 °C. Both phases crystallize in the monoclinic crystal system in the space group *C*2/*c*, exhibiting edge-shared hexagonal "MO_3" (M = Sn or Ti) layers that also contain octahedrally coordinated Li(I)/Cu(I) cations. These layers are bridged by linearly coordinated Cu(I) cations. Magnetic susceptibility measurements confirm the +1 oxidation state of the copper cations. The optical band gaps were found to be indirect and to significantly red shift with the Cu(I) content, down to ∼2.31 eV for **I** and ∼1.46 eV for **II**. Electronic structure calculations show that the decreased band gaps can be attributed to a higher energy valence band derived from the filled $3d^{10}$ orbitals of the Cu(I) cations, which most notably arise from the octahedrally coordinated Cu(I) cations within the layers. Total energy calculations reveal an increasing metastability with respect to decomposition to Cu_2O and SnO_2 or TiO_2 as a result of occupation of the intralayer sites by Cu(I) cations. In both phases, their edge-shared hexagonal layers lead to highly dispersive conduction bands and small electron effective masses of ∼0.51 m_e for **I** and ∼0.41 m_e for **II**. Polycrystalline films of both were deposited onto fluorine-doped tin oxide slides and exhibited *p*-type photocurrents under 100 mW cm^{-2} irradiation in the range of ∼50 to 250 μA cm^{-2}. This study thus reveals new fundamental relationships between the origin of metastability in Cu(I)-oxide semiconductors, i.e., octahedral coordination, and enhanced optical and photoelectrochemical properties.

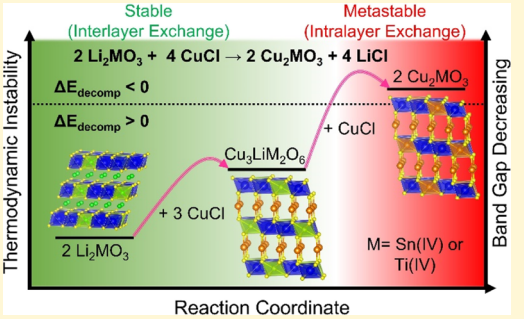

Downloaded via NORTH CAROLINA STATE UNIV on February 22, 2023 at 16:00:43 (UTC).
See https://pubs.acs.org/sharingguidelines for options on how to legitimately share published articles.

INTRODUCTION

Important technological advancements are often underpinned by the ability to discover and synthesize new compounds. This work has led to critical developments in a diverse range of fields, from lithium-ion batteries and photovoltaics/photocatalysis to superconductors and computer data storage. Oftentimes, the greatest scientific breakthroughs can be attributed to the discovery of the "next-best" material. However, as recently highlighted by Cheetham, Seshadri, and Wudl, more often than not these breakthroughs occur with phases that have been repurposed from already-known compounds or were simply previously made out of curiosity.[1] For example, Li_xCoO_2 was initially synthesized and investigated for its magnetic properties in the 1950s, and it was another two decades before its applicability as a cathode for Li-ion batteries was demonstrated by Goodenough and others which eventually led to Goodenough's 2019 Nobel Prize.[2−4] Thus, many of the world's important technological advances can be traced back to the initial synthetic research by solid-state chemists and materials scientists.

Currently, most developed functional materials are based on thermodynamically stable phases, which can be primarily attributed to the fact that conventional solid-state reaction techniques at high temperatures often lead to the formation of only the most thermodynamically stable products. However, it has been postulated that the number of metastable, i.e., thermodynamically unstable, phases greatly exceeds the number of thermodynamically stable ones. Hence, the untapped potential of metastable phases is vast. The challenge lies in the fact that there is still a limited understanding of what factors lead to a metastable solid being synthesizable.[5−7] One hypothesized criterion is that phases with hull energies (i.e., energies above their ground state) that exceed ∼0.1−0.2 eV $atom^{-1}$ should be considered unsynthesizable because they are too thermodynamically unstable. However, recent work has begun to challenge this idea.[8] For example, data-mining studies from Sun and colleagues have revealed the role of cohesive energy in determining the likelihood of a metastable phase's

Received: November 29, 2022
Revised: January 17, 2023
Published: January 27, 2023

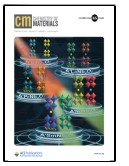

© 2023 American Chemical Society

https://doi.org/10.1021/acs.chemmater.2c03563
Chem. Mater. 2023, 35, 1404−1416

synthesizability, where higher cohesive energies help to "lock-in" energetically unfavorable atomic arrangements and increase synthesizability.[6] Additionally, it was shown that metastable compounds with phase-separated ground states (e.g., AB → *A* + *B*, $\Delta G < 0$), rather than alternate lower energy polymorphs, are often correlated with enhanced synthesizability. This is caused by the fact that phase-separated ground states require bulk-scale ion diffusion and thus have greater kinetic barriers toward decomposition compared to the more local atomic rearrangements needed for a polymorphic transformation. Prior work from our lab has demonstrated how these concepts can be applied in experimental approaches to prepare metastable Sn(II)-perovskite oxides for the first time.[9−11] However, there is the ongoing question of what synthetic techniques are most amenable for the preparation of metastable phases. Therefore, there is still a significant need for fundamental research into the synthesis of metastable phases.

Metastable phases, which rely on kinetic stabilization, are highly unlikely to persist under classical solid-state reaction conditions which require high temperatures in order to facilitate the requisite ion diffusion needed to induce chemical reactions in solids. Consequently, alternative synthetic methods are needed which can circumvent reaction conditions that readily lead to decomposition/transformation to the thermodynamic ground state. A promising synthetic technique is flux-mediated topotactic ion exchange. Flux-based topotactic ion exchange typically involves reacting a precursor compound and a metal salt with a low melting point, whereby the metal cations of the precursor and salt exchange (e.g., $ABO_3 + MX_2 \rightarrow MBO_3 + AX_2$). These reactions are driven by the exothermic formation of the metal halide product (e.g., AX_2) and are able to enable the formation of less stable (i.e., metastable) compounds.[12,13] Several groups, including our own group's work on preparing Sn(II) oxides, have successfully demonstrated the use of these reactions to prepare metastable compounds.[9,14−16] Critically, these reactions allow for more moderate reaction temperatures which are essential for the kinetic stabilization of metastable phases. Additionally, because of the topotactic nature of these reactions, specific structural features can be maintained between the precursor and exchanged product, thereby allowing for the preparation of metastable phases with specific, desirable, structural features. Thus, flux-mediated topotactic ion-exchange reactions are emerging as a versatile technique in the preparation of new metastable phases.

Reported herein, we demonstrate the use of flux-mediated ion-exchange reactions to prepare two new metastable Cu(I) oxide compounds with the compositions Cu_2SnO_3 and $Cu_{2-x}Li_xTiO_3$ that crystallize with delafossite-type structures. Their syntheses are achieved via a low-temperature ion-exchange reaction of Li(I) for Cu(I) cations within the Li_2MO_3 (M = Sn(IV) or Ti(IV)) compounds. Both compounds are related to the parent delafossite structure type but with an additional Cu(I) cation that is octahedrally coordinated within the MO_6 layer. These represent the first known ternary compounds to be prepared in the Cu−Sn−O or Cu−Ti−O phase spaces, which emphasizes how these reactions can be used to prepare even relatively simple metal oxides for the first time. We further show how the presence of the rare intralayer, octahedrally coordinated Cu(I) cations are not only the source of both compounds' thermodynamic instability but also of their significantly reduced band gaps compared to analogous (and thermodynamically stable) Cu(I)-delafossite oxides. This reveals a new fundamental relationship between reduced band gaps and thermodynamic (in)stability in Cu(I)-containing oxides. These features were probed through powder X-ray diffraction, DFT total energy calculations, electronic and band structure calculations, UV−visible diffuse reflectance spectroscopy, and electrochemical impendence spectroscopy. Additionally, initial photoelectrochemical studies show both compounds to be *p*-type photocathodes that are suitable for driving photoelectrochemical reduction of protons to molecular hydrogen under visible light. Finally, we provide context as to how important photocatalytic properties, such as band gaps, band edge potentials, and charge carrier effective masses, are impacted in the new metastable Cu_2SnO_3 and $Cu_{2-x}Li_xTiO_3$ compounds as compared to conventional Cu(I)-delafossites, and which are inextricably linked to their metastable structures. These results are therefore not only relevant to the field of photocatalysis but also more generally demonstrate how metastable compounds have the potential to lead to enhanced physical properties as compared to their thermodynamically stable analogues.

EXPERIMENTAL SECTION

Synthesis of Li_2SnO_3 and Li_2TiO_3. The precursor oxides, Li_2SnO_3 and Li_2TiO_3, were prepared via solid-state reactions using Li_2CO_3 (Fisher Scientific, 99.5%), SnO_2 (Alfa; Aesar, 99.9%), and TiO_2 (J.T. Baker, >99%). Stoichiometric amounts of Li_2CO_3 and SnO_2/TiO_2 were ground together for ∼20 min using a mortar and pestle before being transferred into alumina crucibles. The mixtures were heated in a box furnace to 1100 °C at a rate of 9 °C min^{-1}, held for 12 h, and then allowed to radiatively cool to room temperature within the furnace.

Synthesis of Cu_2SnO_3 and $Cu_{2-x}Li_xTiO_3$. Cu_2SnO_3 was prepared by grinding Li_2SnO_3 (0.451 g) and CuCl (1.98 g-Alfa Aesar, 99%) in a 1:2.2 ratio inside a glovebox under an Ar atmosphere. The mixture was then placed within a fused silica tube and flame-sealed under dynamic vacuum. Subsequently, the ampoule was heated to 475 °C at 11 °C min^{-1} and held for 24 h before being radiatively cooled to room temperature within the furnace. The side products and excess CuCl were removed by first repeatedly washing the products with concentrated ammonium hydroxide, followed by deionized water. The remaining powder was then allowed to dry overnight at 80 °C.

$Cu_{2-x}Li_xTiO_3$ was prepared by grinding Li_2TiO_3 (0.274 g) and CuCl (1.98 g) in a 1:8 ratio inside a glovebox (Ar atmosphere) and then sealed inside a fused silica tube under vacuum. The heating profile and washing procedure were the same as for Cu_2SnO_3. The resulting powder was then subsequently reground with fresh CuCl in 1:8 ratio and reacted a second time following the same procedure. The entire process was repeated for a third and final time to achieve the maximal Cu(I) exchange of ∼80%, or $x \sim 0.4$ for $Cu_{1.6}Li_{0.4}TiO_3$, as described below.

Characterization Techniques. Powder X-ray diffraction (XRD) patterns of all samples were obtained on a Rigaku R-Axis Spider using monochromatic Cu Kα_1 radiation (λ = 1.54056 Å) from a sealed tube X-ray source (40 kV, 36 mA) and a curved image plate detector. Diffraction patterns for refinement were obtained on a PANalytical Empyrean X-ray diffractometer operating with Cu K$\alpha_{1,2}$ radiation (45 kV, 40 mA) and optimizing the sample preparation to avoid preferred orientation. The diffraction patterns were refined using the Rietveld method within the GSAS-II software package.[17] X-ray diffraction patterns for ex situ decomposition experiments were recorded on a Rigaku R-Axis Spider. The ex situ decomposition experiments were performed by sealing powders of Cu_2SnO_3 and $Cu_{2-x}Li_xTiO_3$ into fused silica tubes under vacuum and then placing them into a box furnace at temperatures ranging from 600 to 900 °C for 1 h. After 1 h at the set temperature, the reaction tubes were removed from the

https://doi.org/10.1021/acs.chemmater.2c03563
Chem. Mater. 2023, 35, 1404−1416

furnace and allowed to radiatively cool back to room temperature prior to taking a PXRD measurement of the product.

The magnetic susceptibilities of polycrystalline samples of Cu_2SnO_3 and $Cu_{2-x}Li_xTiO_3$ were measured as a function of temperature and with external magnetic fields of 0.1, 1, and 5 T with a MPMSX7 magnetometer (Quantum Design). The background of the sample holders was determined in separate runs and subtracted from the experimental data. The band gaps and onsets of optical absorption edges were measured using UV−vis diffuse reflectance spectroscopy on a Shimadzu UV-3600 system equipped with an integrating sphere. The data were transformed using the Kubelka−Munk, $F(R)$, function.[18] For photoelectrochemical measurements, polycrystalline films were prepared via drop casting. Films were prepared using ∼20 mg of powder that was dispersed into a *tert*-butanol solution with a small amount of a Nafion binder (5% w/w in water and 1-propanol). The slurry was then drop-cast onto a taped-off 1 cm^2 region of TEC-15 fluorine-doped tin oxide (FTO) slides. The films were then sintered at 500 °C under flowing Ar for 4.5 h and allowed to cool to room temperature under flowing Ar. Electrochemical impedance spectroscopy (EIS) was used to measure the flat band potential and to determine the valence band energies. EIS experiments were run using a frequency of 40 kHz, an AC amplitude of 5 mA, and an applied potential between −1 and +0.4 V versus the normal hydrogen electrode (NHE). A 0.5 M Na_2SO_4 solution served as the electrolyte and was purged with N_2 prior to use. The pH of the solution was measured to be ∼7.0. The Cu_2SnO_3 and $Cu_{2-x}Li_xTiO_3$ films served as the working electrodes, while Pt foil was the counter electrode and a saturated calomel (SCE) (sat. KCl) was the reference electrode. The EIS measurements were taken on a Princeton Applied Research potentiostat (Parstat-2263) using a custom Teflon cell.

Photocurrent measurements were performed using a homemade Teflon photoelectrochemical cell (PEC), where the Cu_2SnO_3 and $Cu_{2-x}Li_xTiO_3$ films served as the working electrode, with a Pt counter electrode and a SCE reference electrode. The data were measured using a Pine Research WaveNow Wireless Potentiostat using a 0.5 M Na_2SO_4 electrolyte solution. The pH of the N_2 purged electrolyte solution was ∼7.0. Linear sweep voltammograms were taken between +0.2 and −0.6 V versus SCE. The light source for the photocurrent measurements was a Xe Arc lamp (Newport Corporation). The films were irradiated with either UV + visible (λ > 230 nm) or visible-only (λ > 400 nm) light. The measured irradiation intensity at the film surface was set to ∼100 mW cm^{-2}. Linear sweep voltammograms were taken under dark and illuminated conditions to determine the photocurrents. Additionally, transient photocurrent measurements were taken by measuring the current under chopped irradiation.

Electronic Structure Calculations. The electronic structures and the total internal energies of the fully exchanged Cu(I), Cu_2SnO_3 and Cu_2TiO_3, and the partially exchanged Cu(I), $Cu_3LiSn_2O_6$ and $Cu_3LiTi_2O_6$, were calculated using density functional theory as implemented in the Vienna Ab Initio Simulation Package (VASP; ver. 4.6). Perdew−Burke−Ernzerhof functionals were used within the generalized gradient approximation.[19,20] The structures were first geometry-relaxed, with 10^{-6} and 10^{-2} eV as the convergence criteria for the total energy and ionic steps, respectively. The Brillouin zone was automatically sampled using a 2 × 2 × 2 Γ-centered *k*-point grid for the geometry relaxation. Next, density of state (DOS) calculations were performed using a finer 8 × 8 × 8 *k*-point grid (144 total *k*-points) for each structure, including projections of the individual atomic orbital contributions. Band structure calculations were also performed across the standard *k*-point paths for their reduced unit cells, i.e., Γ-Y-M-A-Γ and L2- Γ-V2, with 20 *k*-points per reciprocal lattice direction. The resulting band structure diagrams and effective masses were calculated and plotted using the SUMO software package.[21] The thermodynamic stabilities against decomposition to the simpler oxides, e.g., TiO_2, Cu_2O, and SnO_2, were estimated using methods as established previously.[9,22,23] The reaction energies were calculated from the metal oxides and benchmarked for consistency against values found in the Open Quantum Materials Database (OQMD),[24,25] which has been found by total energy calculations within VASP at 0 K.

RESULTS AND DISCUSSION

Synthesis and Structural Characterization. The syntheses of new compounds in the Cu(I)/Sn(IV) and Cu(I)/Ti(IV) oxide systems were investigated by employing a low-temperature reaction of CuCl with the known Li_2SnO_3 and Li_2TiO_3 compounds. Both precursor compounds crystallize in the *C*2/*c* space group and are closely related to the delafossite structure, composed of layers of edge-sharing MO_6 (M = Sn or Ti) and LiO_6 octahedra, as shown in Figure 1 (middle).

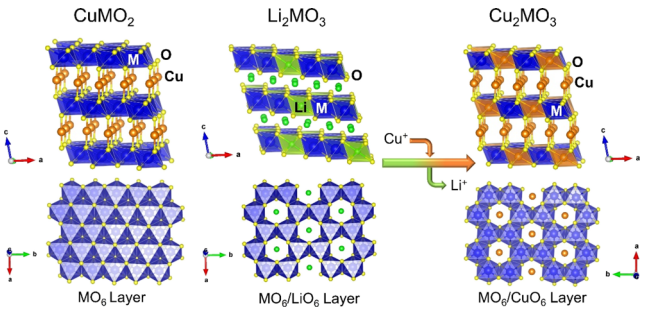

Figure 1. Illustration of $CuMO_2$ (left), Li_2MO_3 (middle), and Cu_2MO_3 (right) crystal structures and their respective octahedral layers. Reaction of Li_2MO_3 with CuCl leads to Cu(I) cation exchange and the new Cu_2MO_3 phases that maintain the mixed MO_6/CuO_6 octahedral layers.

Conventional Cu(I)-delafossites have the chemical formula $Cu^+M^{3+}O_2$ (e.g., M = Al^{+3}, Ga^{+3}, Cr^{+3}, and Fe^{+3}) and are composed of layers of edge-sharing MO_6 octahedra that are bridged by linearly coordinated Cu(I) cations (Figure 1, left). In contrast to the delafossite structure, LiO_6 octahedra in the Li_2MO_3 phases also occur within the hexagonal MO_6 layers. Both Li_2MO_3 precursors were reacted with CuCl under vacuum at 475 °C to attempt to fully exchange Li(I) for Cu(I) cations. The formation of Cu_2SnO_3 was complete after only a single reaction cycle with a near-stoichiometric amount of CuCl, whereas the synthesis of $Cu_{2-x}Li_xTiO_3$ (x_{min} ∼ 0.4) required a 4-fold excess of CuCl and three reaction cycles. While there are clear differences in their cation exchange-abilities, as described in further detail below, the reaction is the same: Li_2MO_3 (M = Sn or Ti) + 2 CuCl → Cu_2MO_3 + 2 LiCl. Upon melting the CuCl reactant, the Cu(I) cations are able to undergo a relatively facile exchange to replace the Li(I) cations while conserving the underlying layered M−O substructure. This reaction is driven by the exothermic formation of LiCl from CuCl, with a calculated ΔH_{calc} = −178 kJ mol^{-1}. This metathesis-type approach has previously been shown to be an effective low-temperature route to prepare metastable solids.[26−28] This helps to offset the energetic penalty of transforming from Li_2MO_3 to Cu_2MO_3, which has ΔH_{calc} = +189 and +216 kJ mol^{-1} for Cu_2SnO_3 and Cu_2TiO_3, respectively. Taken together, the calculated enthalpy changes for the overall reaction are ΔH = +10 kJ mol^{-1} (Cu_2SnO_3) and +38 kJ mol^{-1} (Cu_2TiO_3), which are borderline favorable when considering the associated errors involved with internal energy calculations. At a reaction temperature of 475 °C, CuCl (m.p. ∼425 °C) is a liquid while the solid LiCl product (m.p. ∼600 °C) is formed; thus, there are smaller entropic considerations which are typically unaccounted for in these types of calculations. Additionally, $Cu_{2-x}Li_xTiO_3$ required a significant excess of CuCl and multiple reaction cycles to help drive the maximum Cu(I) cation content into the structure.

https://doi.org/10.1021/acs.chemmater.2c03563
Chem. Mater. 2023, 35, 1404−1416

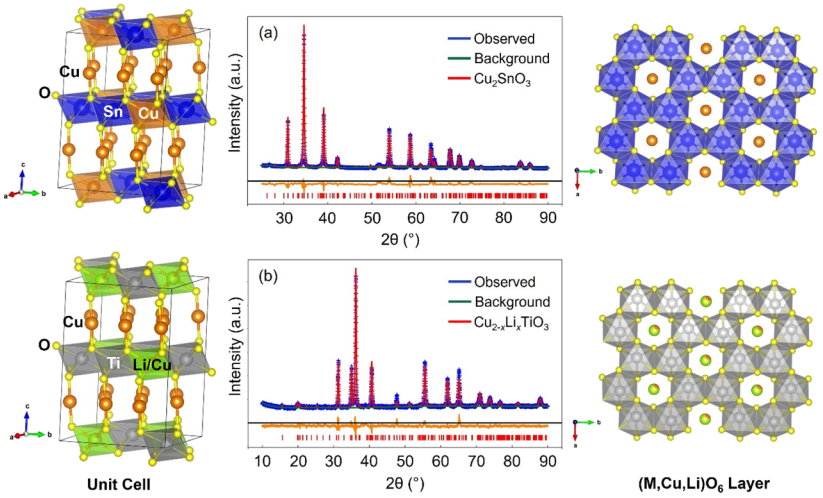

Figure 2. Rietveld refinement plots, middle, for (a) Cu_2SnO_3 and (b) $Cu_{2-x}Li_xTiO_3$. Both adopt the same crystal structure within the *C*2/*c* space group. Unit cell views and octahedral layers are shown to the left and right, respectively.

The crystal structures of the new Cu_2SnO_3 (**I**) and $Cu_{2-x}Li_xTiO_3$ (**II**) compounds were determined by refinement of the powder X-ray diffraction data. Both compounds crystallize in the *C*2/*c* space group and are isostructural to Cu_2IrO_3.[29] The refinement plots and illustrations of the crystal structures are shown in Figure 2. Tables of the refined lattice parameters, atomic positions, site occupancies, and thermal parameters can be found in Tables S1 and S2. Each sample was carefully prepared on the powder XRD sample holder in order to minimize preferred orientation. The structure type consists of four symmetry-unique Cu sites, one Sn/Ti site, and three O sites. The Cu1−Cu3 positions are linearly coordinated and bridging the layers, whereas Cu4 is octahedrally coordinated within the MO_6 layer (i.e., an intralayer Cu site). Both **I** and **II** exhibit similar layers of edge-sharing MO_6 octahedra that are bridged by linearly coordinated Cu(I) cations but deviate from the delafossite structure type by having an additional octahedral Cu site located within the MO_6 layer. This intralayer Cu is a structural feature conserved from the precursor Li_2MO_3, which also has octahedrally coordinated intralayer Li sites. The refined lattice parameters, Tables S1 and S2, for Cu_2SnO_3 are larger than for $Cu_{2-x}Li_xTiO_3$, which is expected given the larger ionic radius for Sn(IV) (0.69 Å) compared to Ti(IV) (0.605 Å). The structural contraction is most apparent in the *ab*-plane containing the MO_6 layers, while changes in the *c*-parameters are less pronounced.

Refinements of the Li/Cu site occupancies revealed that in the titanate compound, the Li(I) cations were not completely replaced with Cu(I) cations. The refinement results show that the intralayer Cu4/Li4 site exchanges up to only ∼20% Cu. This is in contrast to **I**, where the refinements show that a full exchange of Li for Cu has occurred. The refined site occupancies yielded compositions of Cu_2SnO_3 and $Cu_{1.6}Li_{0.4}TiO_3$. The refined Cu to Sn/Ti ratios were consistent with SEM EDS results, Figure S1 and Table S3 in the Supporting Information. These compositions can also be written in standard delafossite notation as $Cu(Cu_{1/3}Sn_{2/3})O_2$ and $Cu(Cu_{0.066}Li_{0.266}Ti_{2/3})O_2$. One possible explanation for the differences in the cation exchangeability of the two compounds is related to the smaller *ab*-plane present in $Cu_{2-x}Li_xTiO_3$ that leads to shorter Cu−O bond distances within the titanate layer. Since the intralayer Cu(I) cations are located in an energetically unfavorable octahedral coordination environment, the more compact titanate layer increases these unfavorable interactions due to the shorter Cu−O bond lengths within the octahedral layer. The octahedral Cu−O bond lengths in Cu_2SnO_3 range between ∼2.01 and 2.11 Å, whereas they are shorter in $Cu_{2-x}Li_xTiO_3$ and range between ∼1.93 and 1.97 Å. Repeated synthetic attempts to fully exchange $Cu_{2-x}Li_xTiO_3$ were unsuccessful and only resulted in the $\sim Cu_{1.6}Li_{0.4}TiO_3$ composition.

As described below, the octahedrally coordinated Cu(I) cations were found to have a key role in determining the optical band gaps of **I** and **II**. As such, synthetic attempts were also made to selectively exchange only the interlayer Li cations, i.e., to yield the more conventional delafossite structure type with only linearly coordinated Cu(I) cations. For the stannate, where exchange is more facile and stoichiometric, the reaction conditions were adjusted for the synthesis of **I** by decreasing the amount of CuCl to give a loaded stoichiometry of $Cu_{1.5}Li_{0.5}SnO_3$, i.e., $Cu_3LiSn_2O_6$. While a prior study has reported a $Cu_3LiSn_2O_6$ (i.e., $CuLi_{1/3}Sn_{2/3}O_2$) compound with preferential interlayer Cu(I) and intralayer Li(I) cations, our reaction resulted in a disordered substitution of Cu(I) cations distributed over both the inter- and intralayer sites.[30] By contrast, the titanate was prepared via reacting Li_2TiO_3 and CuCl in a 1:4 ratio at 475 °C for 24 h for two reaction cycles, yielding $Cu_{1.5}Li_{0.5}TiO_3$ (i.e., $CuLi_{1/3}Ti_{2/3}O_2$) with Cu(I) cations preferentially occupying the interlayer sites. Rietveld refinement of the powder XRD data for both partially exchanged compounds are provided in Figures S2 and S3, and the SEM-EDS results are given in Figure S4 and Table S4 in the Supporting Information.

Magnetic Susceptibility. Considering the uncommon octahedral coordination of the intralayer Cu(I) cations, magnetic susceptibility measurements were collected to probe their oxidation states. Plotted in Figure 3 are the molar magnetic susceptibilities of **I** and **II** versus the inverse temperature, with both showing consistency with a Curie or Curie−Weiss behavior (eq 1)

$$\chi_{mol}(T) = \chi_0 + x_{imp}\frac{C}{T - \Theta_{CW}} \quad (1)$$

https://doi.org/10.1021/acs.chemmater.2c03563
Chem. Mater. 2023, 35, 1404−1416

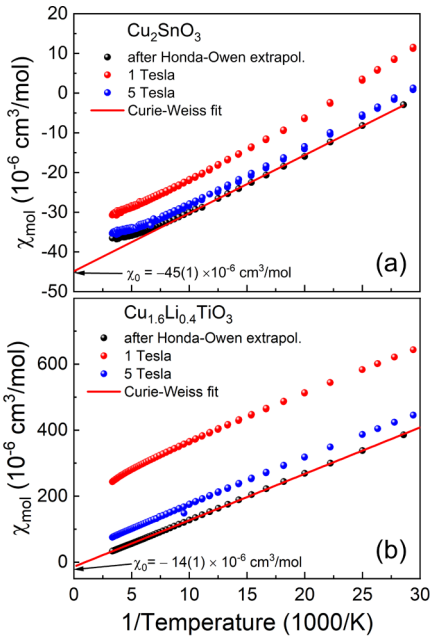

Figure 3. Magnetic susceptibilities of (a) **I** and (b) **II** as a function of reciprocal temperature measured at magnetic fields of 1 Tesla and 5 Tesla. The black solid circles indicate the results of the Honda−Owen extrapolation. The solid red lines are fits using eq 1 with temperature-independent magnetic susceptibilities X_0 as indicated. The slopes correspond to 0.4 and 3.8% of paramagnetic spin $S = 1/2$ impurities for **I** and **II**, respectively.

where χ_{mol} represents the molar susceptibility of paramagnetic cations, with spin S and C being the Curie constants given by

$$C = \frac{N_A g^2 \mu_B^2 S(S+1)}{3k_B} \quad (2)$$

with N_A being Avogadro's constant, g_{mon} the g-factor, μ_B the Bohr magneton, S the spin, and x_{imp} the concentration of the magnetic centers.

A Curie−Weiss temperature Θ_{CW} is included to take account of possible weak exchange coupling between the magnetic centers. The slopes of the susceptibilities versus $1/T$ are noticeably different, indicating significantly different magnitudes of x_{imp} for both samples. In addition to the temperature dependence, the susceptibilities decrease with increasing magnetic field, which are attributed to increasing saturation with higher magnetic fields of minute traces of ferromagnetic impurities. Using a Honda−Owen extrapolation ($\mu_0 H \to \infty$),[31,32] the data were corrected for the ferromagnetic impurities and obtained magnetic susceptibilities which fit well to eq 1 with $x_{imp} = 3.8\%$ ($\Theta_{CW} = -2$ K) and 0.4% ($\Theta_{CW} \approx 0$ K) for $Cu_{2-x}Li_xTiO_3$ and Cu_2SnO_3, respectively, assuming the most unfavorable case of $S = 1/2$ entities and a g-factor of 2. Impurities with larger spin values reduce x_{imp} according to eq 2. The temperature-independent diamagnetic susceptibilities χ_0 amount to -45×10^{-6} cm^3 mol^{-1} and -14×10^{-6} cm^3 mol^{-1} for **I** and **II**, respectively, consistent with the sum of the diamagnetic susceptibility increments of the electrons in the closed shells of the ions (Li^+: -12×10^{-6} cm^3 mol^{-1}, Cu^+: -12×10^{-6} cm^3 mol^{-1}, Ti^{4+}: -5×10^{-6} cm^3 mol^{-1}; Sn^{4+}: -16×10^{-6} cm^3 mol^{-1}; and O^{2-}: -12×10^{-6} cm^3 mol^{-1}).[33] In summary for **I** and **II**, magnetic susceptibility measurements indicate that both are diamagnetic compounds with Cu in the +1 oxidation state. The weak paramagnetism observed in the samples can be casually attributed to small traces of paramagnetic impurities of a few percent or less.

Metastability Properties. The thermodynamic stabilities of both **I** and **II** were interrogated via ex situ powder XRD and total internal energy calculations. The ex situ XRD data were taken by heating the compounds under vacuum to temperatures between 600 and 900 °C for 1 h. Powder XRD patterns were taken in 100 °C intervals. The results are shown in Figure S6a,b for Cu_2SnO_3 and $Cu_{2-x}Li_xTiO_3$, respectively. **I** was found to be stable up to ∼700 °C, while at ∼800 °C, Bragg reflections corresponding to Cu_2O and SnO_2 begin to appear. Further heating at 900 °C leads to complete decomposition, with the observed diffraction peaks corresponding to only Cu_2O and SnO_2. Similarly, **II** was found to be stable up to ∼700 °C but completely decomposed into one or more unknown products at ∼800 °C. While both compounds were found to be thermodynamically unstable, or metastable, each clearly shows a sizable kinetic stabilization. Despite being synthesized at only 475 °C, both compounds are able to reach temperatures up to ∼700 °C before there is sufficient ion diffusion for their bulk-scale decomposition by phase segregation into simpler oxides. These results are in keeping with recent studies that suggest metastable phases which decompose via phase segregation are potentially more synthesizable as they must overcome large kinetic barriers to bulk-scale ion diffusion.[6,9−11] This also demonstrates the effectiveness of low-temperature ion-exchange reactions in the preparation of new, metastable semiconductors.

Using methods established in prior studies,[9,22,23] the thermodynamic stabilities of **I** and **II** were also investigated through calculations of reaction decomposition energies from the calculated internal energies of Li_2SnO_3, Li_2TiO_3, Cu_2SnO_3, $Cu_{2-x}Li_xTiO_3$, and their constituent binary oxides (e.g., Li_2O, Cu_2O, SnO_2, and TiO_2). Prior work by Hautier et al. has shown that formation energies of metal oxides at 0 K can be accurately estimated by their total energies, with a mean deviation close to zero and standard deviation of only ∼24 meV atom^{-1}.[22] The reaction decomposition energies were similarly calculated for **I** and **II** to give the binary oxides (e.g., $Cu_2SnO_3 \rightarrow Cu_2O + SnO_2$). For simplicity, $Cu_{2-x}Li_xTiO_3$ was modeled as the fully exchanged phase Cu_2TiO_3. A positive ΔE_{decomp} indicates that the decomposition is thermodynamically unfavorable while a negative value implies that decomposition is favorable. The calculated total internal energies and ΔE_{decomp} for the stannate and titanate compounds are depicted in Figure 4a,b. The Li_2SnO_3 and Li_2TiO_3 precursors were both stable versus decomposition, with a ΔE_{decomp} of +0.73 and +1.35 eV, respectively, consistent with the high-temperature solid-state synthesis method that is employed in their preparation.

As a first step, the metastability of the partially Cu(I)-exchanged delafossite structures was calculated, i.e., $Cu_3LiM_2O_6$ (M = Sn and Ti), containing only the linearly coordinated Cu(I) cations between the layers. For **I**, the exchange of only the interlayer sites for Cu was found to decrease the stannate's total energy from −5.89 eV atom^{-1} in Li_2SnO_3 to −5.72 eV atom^{-1} in $Cu_3LiSn_2O_6$ (labeled 2a in Figure 4a). In turn, this led to a decreased thermodynamical stability for $Cu_3LiSn_2O_6$, with a positive ΔE_{decomp} of +0.60 eV, shown in Figure 4a. Therefore, while the delafossite analogue of the stannate structure is less stable than the precursor Li_2SnO_3, this is a thermodynamically stable phase. For **II**,

https://doi.org/10.1021/acs.chemmater.2c03563
Chem. Mater. 2023, 35, 1404−1416

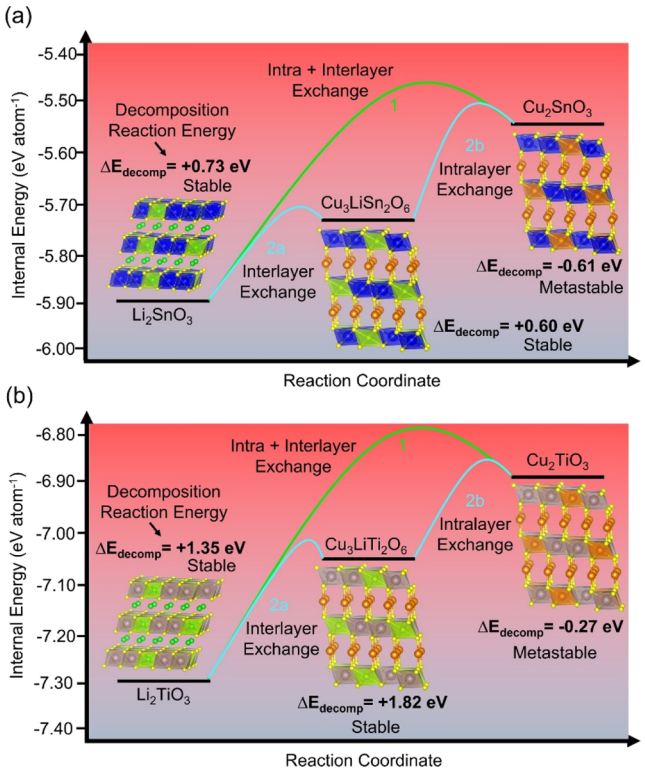

Figure 4. Calculated internal and decomposition energies for the (a) stannate and (b) titanate systems. Decomposition energies are calculated for **I** (upper) and **II** (lower) with respect to their constituent binary oxides and labeled ΔE_{decomp}. A positive value indicates that the compound is stable, while a negative value indicates that it is metastable. Calculations show that both are metastable with the intralayer, octahedrally coordinated Cu(I) cations being the high-energy structural feature.

shown in Figure 4b, substitution of the interlayer sites for Cu results in a decrease of the titanate's total energy from −7.27 eV atom^{-1} to −7.05 eV atom^{-1}. However, this yields an increased thermodynamic stability of +0.47 eV with a ΔE_{decomp} of +1.82 eV. While this may seem counterintuitive, the decomposition of **II** leads to TiO_2 rather than SnO_2. Consequently, while the $Cu_3LiTi_2O_6$ structure is higher in energy than Li_2TiO_3, this is more than offset by its less stable combination of decomposition products. Thus, the Cu(I) cation exchange of the interlayer sites with the linear coordination geometries results in thermodynamically stable compounds in both cases.

As a next step, the metastabilities of the fully Cu(I)-exchanged structures were calculated for both **I** and **II**. For the stannate structure of **I**, the addition of intralayer Cu(I) cations causes the energy of the compound to substantially increase by +0.15 eV atom^{-1} to −5.57 eV atom^{-1} for Cu_2SnO_3, labeled 2b in Figure 4a . At this point, the compound has become thermodynamically unstable with respect to the binary oxides, with a negative ΔE_{decomp} of −0.61 eV, as a result of the octahedrally coordinated Cu(I) cations. Similarly, for the titanate structure of **II**, the total energy of Cu_2TiO_3 has increased to −6.90 eV atom^{-1}. Analogous to the stannate system, the addition of the intralayer, octahedrally coordinated, Cu sites pushes the structure into the metastable regime with a ΔE_{decomp} value of −0.27 eV. The calculations clearly show that the structural feature which renders both Cu_2SnO_3 and $Cu_{2-x}Li_xTiO_3$ metastable are the intralayer Cu(I) cation sites that are octahedrally coordinated. It is well known that Cu(I) prefers a linear coordination environment owing to its closed-shell d^{10} electron configuration, with any oxygen−ligand interactions resulting in antibonding interactions that raise the energy of its d-orbital electrons. For instance, linearly coordinated Cu(I) cations located in the interlayer sites only interact with the oxygen anions via their d_{z^2} orbital with two antibonding interactions. However, the octahedrally coordinated Cu(I) at the intralayer sites have six antibonding interactions with its $3d_{z^2}$ orbital and four antibonding interactions with its $3d_{x^2-y^2}$ orbital. This is also reflected by the structure of prototypical Cu(I)-delafossites that only contain linearly coordinated Cu(I) cations and tend to be thermodynamically stable. Similarly, the decomposition energies for the delafossite analogues, $Cu_3LiSn_2O_6$ and $Cu_3LiTi_2O_6$, are calculated to be thermodynamically stable versus their binary oxides. As described earlier, a likely explanation for the lack of a full Cu(I) cation exchange in **II** is that the Cu(I) cations are being forced into a smaller octahedral coordination environment as compared to Cu_2SnO_3 and consequently more strongly disfavoring intralayer exchange.

An additional factor accounting for the different Cu(I) cation exchangeabilities between **I** and **II** is also likely in the relative thermodynamic stabilities of the reaction intermediates, e.g., $Cu_3LiM_2O_6$ for each. There are three potential reaction pathways for the Cu(I) cations in these compounds: (1) disordered exchange of both the inter- and intralayer simultaneously, (2) preferential exchange of the interlayer, followed by the intralayer cation sites, or (3) preferential exchange of the intralayer, followed by the interlayer. Based on the observed difficulty in exchanging the intralayer sites in **II**, and the unfavorable octahedral coordination, pathway 3 can be ruled out. The attempted syntheses of the partially exchanged $Cu_3LiSn_2O_6$ and $Cu_3LiTi_2O_6$ delafossites show that the stannate undergoes a disordered exchange of Cu(I), pathway 1, while the titanate preferentially exchanges the interlayer sites, pathway 2. This reaction pathway variability is likely related to the different relative thermodynamic stabilities of the $Cu_3LiM_2O_6$ intermediates. When considering that the interlayer cations are likely more exchangeable, it is probable that the titanate first reacts to form the $Cu_3LiTi_2O_6$ composition, which is the thermodynamic minimum for the entire reaction pathway (i.e., $Cu_3LiTi_2O_6$ is more stable than either Li_2TiO_3 or Cu_2TiO_3). To complete the exchange, not only must the system overcome the kinetic barrier to exchange the remaining intralayer sites but also escape from the reaction's global thermodynamic minimum. Conversely, $Cu_3LiSn_2O_6$ is not the thermodynamic minimum, and the reaction is not kinetically trapped at this intermediate and complete exchange can be achieved.

Electronic Structure Calculations. The electronic structures of conventional Cu(I)-delafossites have been well studied. Their valence bands are formed via the filled Cu $3d^{10}$ orbitals while the conduction bands are derived from the empty orbitals of either the main group or transition metal cations on the B site.[34,35] Results of calculations on the partially exchanged $Cu_3LiM_2O_6$ delafossite analogues follow a similar trend, as shown in the DOS plots for $Cu_3LiSn_2O_6$ and $Cu_3LiTi_2O_6$ in Figure 5a,b, respectively. The tops of the valence bands are mostly composed of Cu 3*d* states with minor contributions from O 2*p* orbitals. Since the $Cu_3LiM_2O_6$ phases do not contain any intralayer Cu, the Cu-based states at the

https://doi.org/10.1021/acs.chemmater.2c03563
Chem. Mater. 2023, 35, 1404−1416

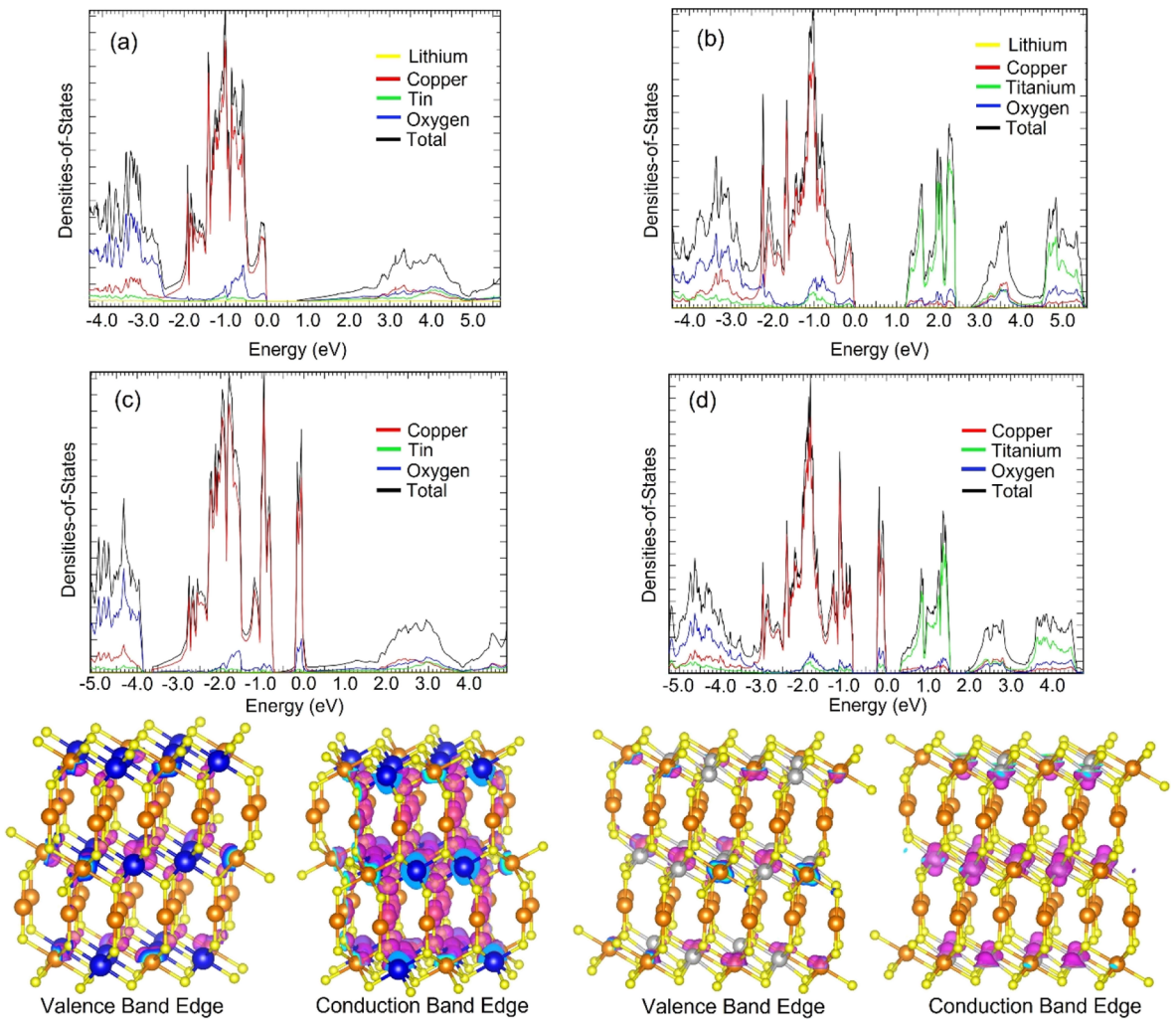

Figure 5. Calculated DOS for (a) $Cu_3LiSn_2O_6$, (b) $Cu_3LiTi_2O_6$, (c) Cu_2SnO_3, and (d) Cu_2TiO_3. Projected electron densities, purple colored, for the upper-most 0.5 eV portion of the valence band edge and lower 0.5 eV portion of the conduction band edge for **I** and **II** are shown below their respective DOS plots.

valence band edge stem from the interlayer Cu. The conduction band of $Cu_3LiTi_2O_6$ is primarily formed from empty Ti 3*d* orbitals, though there are minor contributions from O 2*p* and Cu 4*s* orbitals as well. Conversely, the conduction band of $Cu_3LiSn_2O_6$ is a combination of Sn 5*s* and 5*p* orbitals mixed with O 2*p*. The conduction band of $Cu_3LiSn_2O_6$ is much more disperse than for $Cu_3LiTi_2O_6$, which is a common feature in Sn(IV)-containing oxides. This dispersion is caused by the stronger σ^* interactions of the Sn *s*- and p-orbitals compared to the weaker π^* interactions of transition metal d-orbitals.[36,37] The Li(I) cations make no contributions to either the valence or conduction band edge states.

The key structural difference between conventional delafossites and **I** and **II** is the presence of intralayer Cu(I) cations and would be expected to qualitatively change their electronic structures. The calculated DOS plots for Cu_2SnO_3 and Cu_2TiO_3 are shown in Figure 5c,d. The electronic structure for Cu_2TiO_3 will be representative of $Cu_{2-x}Li_xTiO_3$ due to the presence of the intralayer Cu(I) cations in both phases. In both **I** and **II**, new and significantly higher valence band states were found. This narrow set of new states occurs at the top of the valence band between 0.0 and −0.3 eV. The projected electron density for this region for both Cu_2SnO_3 and Cu_2TiO_3 are depicted below their respective DOS plots. As can be seen, the electron density for the valence band edge is delocalized over the intralayer Cu(I) cations. Additionally, the predicted band gaps for each compound have dramatically decreased. The calculated band gap for Cu_2TiO_3 decreases by ∼0.9 eV compared to $Cu_3LiTi_2O_6$. In the case of Cu_2SnO_3, the band gap shrinks by ∼0.7 eV with the absence of a clear gap. In both Cu_2TiO_3 and Cu_2SnO_3, the calculated band gap energies are significantly underestimated compared to the experimental values (shown below). The underestimation of the band gap energies is a well-known issue in DFT calculations, and particularly so for phases with conduction bands derived from main group elements such as Sn(IV).[38] Therefore, the relative changes in the band gaps upon the addition of the intralayer Cu(I) cations are more insightful than the absolute values of the band gaps. The addition of the intralayer Cu(I) cations are shown to dramatically decrease the band gap energies, which, in turn, can facilitate broader range visible light absorption. The intralayer Cu(I) cations are not found in more conventional Cu(I)-delafossites, which is, in fact, the structural feature leading to the metastability in each case. Hence, a clear relationship is revealed between the metastable structural

https://doi.org/10.1021/acs.chemmater.2c03563
Chem. Mater. 2023, 35, 1404−1416

feature of Cu_2SnO_3 and $Cu_{2-x}Li_xTiO_3$ and their smaller band gaps.

By comparison, conduction band states of **I** and **II** are essentially unaltered with respect to their respective delafossite analogues. Depictions of the projected electron density for the bottom 0.5 eV portion of the conduction band are shown below the DOS plots. The electron density for **II** is delocalized almost exclusively over the Ti(IV) cations, with minor contributions from the interlayer Cu and O. In the case of **I**, the conduction band electron density is complicated by the predicted lack of a band gap. The projected electron density is better reflected in the DOS calculated for $Cu_3LiSn_2O_6$, where the conduction band edge only has contributions from Sn and O and effective masses can be determined. The electron density at each of the band edges shows that the lowest energy electronic transitions stem from excitations between the intralayer Cu(I) $3d^{10}$ states and the empty Sn $5s^0/5p^0$ or Ti $3d^0$ states in **I** and **II**, respectively.

The calculated band structures at the band edges for **I** and **II** are plotted in Figure 6, and the corresponding effective masses

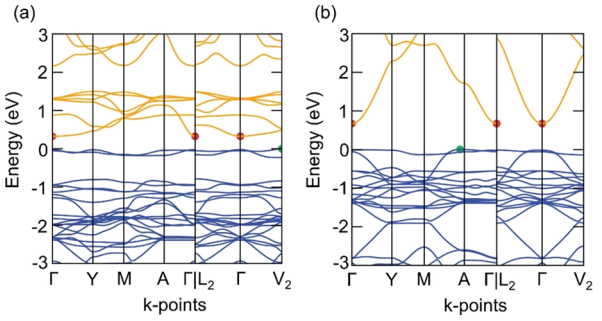

Figure 6. Calculated band structures of (a) Cu_2TiO_3 and (b) $Cu_3LiSn_2O_6$. The valence band states are shown in blue and the conduction bands states are plotted in yellow. The valence band maximum is labeled by a green dot, while the conduction band minimum is indicated by a red dot.

Table 1. Calculated Electron and Hole Effective Masses for Cu_2TiO_3 and $Cu_3LiSn_2O_6$

		electron effective mass	
compound	hole effective mass	min	max
Cu_2TiO_3	2.98 ($V_2 \rightarrow \Gamma$)	0.41 ($\Gamma \rightarrow$ A)	12.89 ($\Gamma \rightarrow$ Y)
$Cu_3LiSn_2O_6$	2.19 (A $\rightarrow$ M)	0.51 ($\Gamma \rightarrow$ A)	0.62 ($\Gamma \rightarrow V_2$)

are listed in Table 1. For the band structure of **II**, Cu_2TiO_3, the conduction band shows a moderate dispersion that is consistent with the band structures of related metal oxides that are derived from transition metal d-orbitals. Conversely, the narrow set of bands at the top of the valence band are those of the intralayer Cu(I) cations, which are relatively flat as compared to the conduction band. The bands deeper within the valence band, derived from the interlayer Cu(I), are only marginally more disperse than the higher energy intralayer bands. Figure 6b shows the band structure for $Cu_3LiSn_2O_6$, with a large dispersion of the conduction band of ~2.5 eV as can be found for some Sn(IV) oxides.[39,40]

Along their most disperse directions, both semiconductors show relatively small electron effective masses of 0.41 and 0.51 m_e for **II** and **I**, respectively. Both of these values are substantially smaller than the calculated electron effective masses in $CuFeO_2$ of 1.83 m_e,[41] which has been considered the most promising Cu(I)-delafossite photocathode. The small electron effective masses found in **I** and **II** are critical for obtaining the large minority carrier diffusion lengths that are an important feature for obtaining high photocatalytic/photoelectrochemical efficiencies. One significant difference is in the greater anisotropy of the effective masses of **II**. While $Cu_3LiSn_2O_6$ has small electron effective masses in every calculated direction, the Cu_2TiO_3 structure only has a small electron effective mass along a single calculated direction. Consequently, Cu_2TiO_3 would be expected to show highly anisotropic electron mobilities. For the valence bands of both **I** and **II**, the hole effective masses are relatively higher as compared to the electron effective masses, although they are comparable to other Cu(I)-delafossites. For instance, the $Cu_3LiSn_2O_6$ delafossite analogue has a hole effective mass of 2.19 m_e, while the hole effective mass of the transparent conducting oxide (TCO) $CuAlO_2$ has a calculated hole effective mass of 1.9 m_e.[42] The hole effective mass for Cu_2TiO_3 is higher at 2.98 m_e. The higher effective mass in Cu_2TiO_3 likely arises from the fact that the intralayer Cu(I) sites are isolated and not bridged into extended -Cu−O−Cu−O- pathways needed for significant band dispersion. However, their hole effective masses are at least comparable to other Cu(I)-delafossites, which have been investigated as *p*-type photocathodes and TCOs. The origin of the high conductivities in Cu(I)-delafossite TCOs has been attributed to high carrier concentrations and doping concentrations rather than having exceptionally low hole effective masses. For example, 5% Mg doping into $CuCrO_2$ has been shown to increase its conductivity by 2 orders of magnitude.[43]

Optical Band Gap and Band Edge Energies. The optical band gaps for **I** and **II** were measured via UV−vis diffuse reflectance spectroscopy. Tauc plots of the indirect and direct transitions are shown in Figure 7. Both compounds have

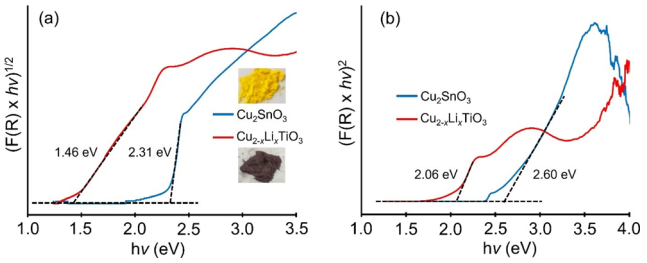

Figure 7. Tauc plots of the UV−visible diffuse reflectance data for Cu_2SnO_3 and $Cu_{2-x}Li_xTiO_3$ for (a) indirect transition and (b) direct transition gaps. Inset in (a) are optical images of each compound in powder form.

a lowest energy indirect transition of 2.31 and 1.46 eV for Cu_2SnO_3 and $Cu_{2-x}Li_xTiO_3$, respectively. The insets in Figure 7a show the images of the compounds in powder form. Cu_2SnO_3 appears as a vibrant yellow color, while $Cu_{2-x}Li_xTiO_3$ is black to dark brown. The direct transitions for both compounds are at higher energies. The direct transition for Cu_2SnO_3 was measured to be 2.60 eV, while the direct transition for $Cu_{2-x}Li_xTiO_3$ was found at 2.06 eV. The measured band gaps are significantly greater than those calculated as described above. However, these band gaps are significantly smaller than those reported for other Cu(I)-delafossites. An illustrative comparison is between Cu_2SnO_3

https://doi.org/10.1021/acs.chemmater.2c03563
Chem. Mater. 2023, 35, 1404−1416

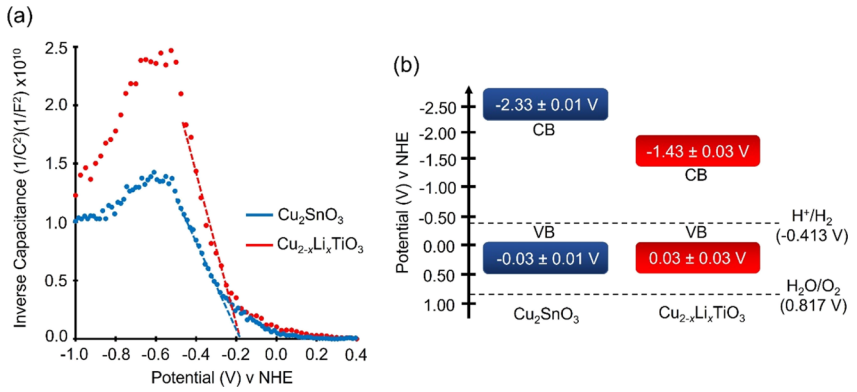

Figure 8. (a) Plot of the inverse square of the capacitance versus applied bias for films of Cu_2SnO_3 and $Cu_{2-x}Li_xTiO_3$. The extrapolated flat band potentials are indicated by dashed lines. (b) Valence and conduction band edge energies of Cu_2SnO_3 and $Cu_{2-x}Li_xTiO_3$ with respect to NHE and the proton reduction and water oxidation potentials at pH = 7.

and the family of $CuMO_2$ (M = Al, Ga, and In) compounds. The B-site cations for the $CuMO_2$ family come from group 13, directly next to Sn (group 14), with conduction bands derived from their empty s and p orbitals. The measured band gap energies for these compounds are significantly larger ~3.5 eV ($CuAlO_2$), ~3.6 eV ($CuGaO_2$), and ~3.9 eV ($CuInO_2$).[44] By comparison, diffuse reflectance measurements on the partially Cu(I)-exchanged titanate version, that is, the $Cu_3LiTi_2O_6$ delafossite (Figure S5a), shows a larger band gap of ~2.0 eV as compared to the more fully exchanged **II** of ~1.46 eV. This trend is the result of the exchange of first the interlayer and then the intralayer Cu(I) cations, causing a stepwise red shift of its band gap. Conversely, for the stannate, the Cu(I) cations exchange simultaneously at all crystallographic sites, so the red shift occurs down to ~2.3 eV without any intermediates. This trend again highlights the role of the metastable structural features, i.e., the intralayer, octahedrally coordinated Cu(I) cations, in leading to a significantly red-shifted band gap.

The valence band edge energies of **I** and **II** were also measured via Mott−Schottky experiments. A detailed explanation of Mott−Schottky experiments and the relevant equations have been reported previously.[45,46] Shown in Figure 8a are plots of the inverse of the dielectric capacitance squared versus the applied bias for polycrystalline films of **I** and **II** after deposition onto FTO slides. Both semiconductors show a clear *p*-type response with nearly similar flat band potentials of about −0.2 V. The flat band potentials were used to calculate the valence band energies according to methods reported previously. The valence band potentials for Cu_2SnO_3 and $Cu_{2-x}Li_xTiO_3$ were measured to be −0.03 ± 0.01 and +0.03 ± 0.03 V versus NHE at pH 7, respectively, Figure 8b. The similar valence band edge energies were expected given that the top of the valence band for both compounds are derived from the intralayer Cu(I) states in each structure. The conduction band edge energies were next determined using the measured band gaps and are located at −2.33 ± 0.01 V for Cu_2SnO_3 and −1.43 ± 0.03 V for $Cu_{2-x}Li_xTiO_3$, Figure 8b.

The band edge energies are shown in Figure 8b alongside the electrochemical potentials for the water splitting reactions. The high energy valence band edges make them unsuitable for water oxidation. However, their conduction band edges are suitable for driving photocatalytic reduction reactions. The valence band edges for both compounds are high relative to typical valence band energies of other Cu(I) oxides. For example, the valence band energies of several other Cu(I)-delafossites have been measured and range between +0.54 and +0.9 V with an average valence band energy of about +0.7 V versus NHE at pH 7.[47] Thus, both **I** and **II** have substantially higher energy valence bands as compared to conventional Cu(I)-delafossites. Based on the electronic structure calculations, the intralayer Cu(I) cations cause the valence band edges of **I** and **II** to increase by ~0.7 and ~0.9 eV, respectively, with respect to $Cu_3LiM_2O_6$ (M = Sn and Ti). Additionally, the measured band gaps of **II** and $Cu_3LiTi_2O_6$ show a decrease of ~0.6 eV. Thus, the valence band energies for **I** and **II** should be expected to be ~0.6−0.9 eV higher than in conventional Cu(I)-delafossites. Given that the average valence band energy for Cu(I)-delafossites was about +0.7 V, this places the expected valence band energies of **I** and **II** at about +0.1 to −0.2 V. The valence band edge energies of ~0.0 V for both are firmly within this expected range.

Photocatalytic Activity as Polycrystalline Films. Generally, Cu(I) oxide *p*-type semiconductors have been extensively studied as photocathodes.[48−52] As *p*-type semiconductors, photogenerated electrons within the semiconductor's space charge layer are driven to the film surface where they can be used to drive reduction reactions. Accordingly, polycrystalline films of **I** and **II** were investigated as photocathodes by drop-casting their powders onto FTO substrates, followed by annealing under Ar at 500 °C. These films served as the working electrode in a three-electrode setup, with a Pt counter electrode and a saturated calomel (SCE in sat. KCl) reference electrode. The experiments were performed using a 0.5 M Na_2SO_4 aqueous solution as the electrolyte. The films were irradiated with either UV + visible (λ > 230 nm) or visible-only (λ > 400 nm) light with the irradiation power set to ~100 mW cm^{-2}. Plots of the current versus applied bias for Cu_2SnO_3 (Figure S7a) and $Cu_{2-x}Li_xTiO_3$ (Figure S7b) films under UV + visible irradiation show modest *p*-type photocurrents in the range of ~3 and ~6 μA cm^{-2} at −0.6 V versus SCE, respectively. The $Cu_{2-x}Li_xTiO_3$ film exhibits a low onset potential of ~0.0 V, while the onset potential of Cu_2SnO_3 is slightly higher at about −0.12 V. The lower onset potential for $Cu_{2-x}Li_xTiO_3$ suggests that the charge separation is better in $Cu_{2-x}Li_xTiO_3$ compared to Cu_2SnO_3. Both films also show a significant amount of dark current, which is not uncommon for Cu(I) oxides owing to their tendency to corrode at the surfaces.[53,54]

Small photocurrents for pristine, that is, bare surface films with no co-catalyst, for Cu(I) oxide films are commonly

https://doi.org/10.1021/acs.chemmater.2c03563
Chem. Mater. 2023, 35, 1404−1416

observed. It has been suggested that the bare surfaces of Cu(I) oxide films are poorly catalytic and results in significant charge recombination and/or photocorrosion of Cu(I) to Cu(0).[55] However, several studies have demonstrated that moderate oxidation of Cu(I) oxide films produces nano-islands of "CuO" at the particles' surfaces, which can greatly improve the measured photocurrents.[56−58] The proposed mechanism of the enhancement is due to a favorable type-II band offset between the Cu(I) oxide film and CuO. As shown in Figure 9, a type-II

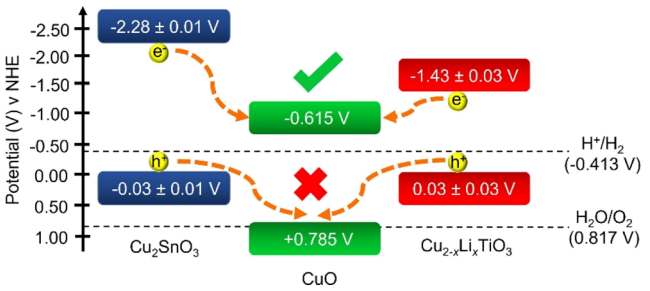

Figure 9. Schematic of the type-II band offset that is formed between $Cu_2SnO_3/Cu_{2-x}Li_xTiO_3$ and CuO. The conduction band of CuO is below that of the Cu(I) oxides and facilitates electron transfer from the Cu(I) oxide films to the CuO at the film surface. The valence band energy of CuO is at more positive potentials compared to the Cu(I) oxides, which prevents hole transfer to CuO.

band offset would also develop between $Cu_2SnO_3/Cu_{2-x}Li_xTiO_3$ and CuO. The conduction band energies of Cu_2SnO_3 and $Cu_{2-x}Li_xTiO_3$ are higher than the conduction band of CuO and leads to the transfer of photogenerated electrons from $Cu_2SnO_3/Cu_{2-x}Li_xTiO_3$ to CuO. On the other hand, the valence bands of $Cu_2SnO_3/Cu_{2-x}Li_xTiO_3$ are at more negative potentials than CuO and therefore inhibits the photogenerated holes from being likewise transferred to CuO.

Polycrystalline films of **II** were oxidized by heating in air at 400 °C for 30 min, following previously reported procedures,[56] and the resulting photocurrents of these films are plotted in Figure 10. Additional plots of the photocurrents under chopped irradiation are displayed in Figure S8. Figure 10a shows that the photocurrent of the oxidized film under UV + visible irradiation has increased from ∼6 to ∼147 μA cm^{-2} at −0.6 V. Furthermore, under chopped UV + visible irradiation (Figure S8a), it can be seen that the photocurrent onset is shifted slightly more positive to ∼+0.1 V. Under visible-only irradiation, Figure 10b, the generated photocurrent decreases compared to combined UV + visible irradiation. The maximum photocurrent under visible-only irradiation was measured to be ∼21 μA cm^{-2} at −0.6 V, with an onset potential of ∼+0.1 V.

Similar attempts to oxidize polycrystalline films of **I** were not as successful. Instead, CuO was deposited onto Cu_2SnO_3 by dropping small amounts (∼5 drops) of 0.25 M $Cu(NO_3)_2$ onto the film surface, followed by heating at 250 °C for 20 min, in accordance with prior studies.[56] The addition of CuO onto the surface of Cu_2SnO_3 resulted in similarly enhanced photocurrents, plotted in Figure 11. The maximum photocurrent for CuO−Cu_2SnO_3 under UV + visible irradiation was ∼92 μA cm^{-2} at −0.55 V. This represents an increase of ∼89 μA cm^{-2} as compared to the pristine film. Irradiation from visible-only light resulted in a maximum photocurrent of ∼61 μA cm^{-2} at −0.53 V. Similar plots of the CuO−Cu_2SnO_3 photocurrents under chopped irradiation are shown in Figure S9. The plots for the chopped irradiation show that the onset

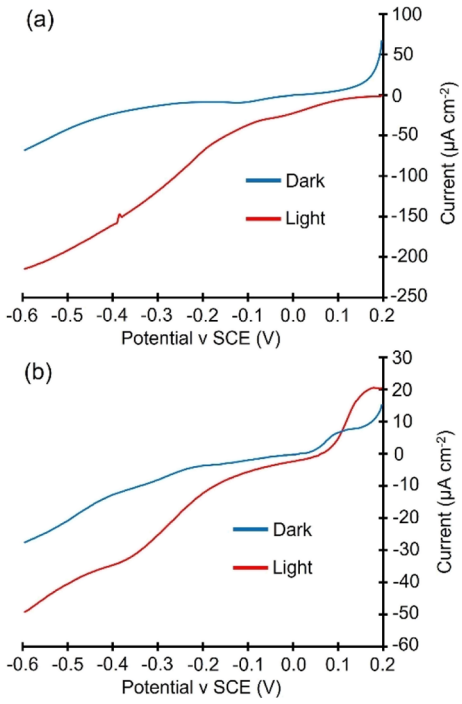

Figure 10. Graphs of the measured current versus applied potential for films of $Cu_{2-x}Li_xTiO_3$ oxidized at 400 °C for 30 min. The photocurrents are determined by subtracting the current measured in the dark from the current obtained under illumination. Wavelengths of light were (a) UV + visible (λ > 230 nm) and (b) visible only (λ > 400 nm) at ∼100 mW cm^{-2}.

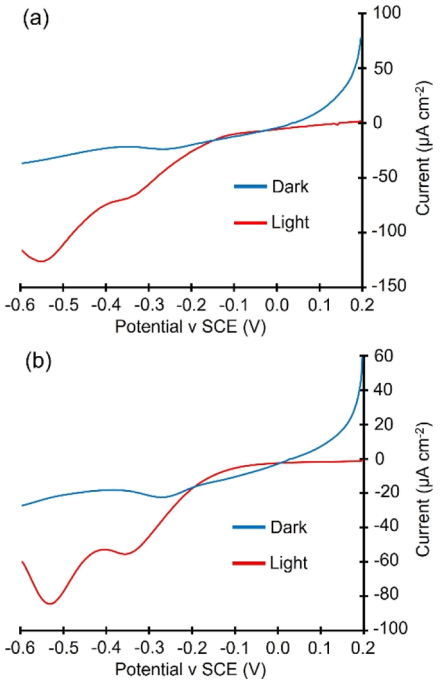

Figure 11. Graphs of the measured current versus applied potential for films of CuO−Cu_2SnO_3. The photocurrents are determined by subtracting the current measured in the dark from the current obtained under illumination. Wavelengths of light were (a) UV + visible (λ > 230 nm) and (b) visible only (λ > 400 nm) at ∼100 mW cm^{-2}.

of photocurrent for the CuO−Cu_2SnO_3 films is at ∼+0.12 V under UV + visible and at 0.0 V under visible only, which are

https://doi.org/10.1021/acs.chemmater.2c03563
Chem. Mater. 2023, 35, 1404−1416

more positively shifted compared to films with bare surfaces. Additionally, films of pure CuO were prepared in an identical fashion to the CuO−Cu_2SnO_3 films, although CuO was directly on an FTO substrate with no Cu_2SnO_3. Measurements of the CuO films (Figure S10) only showed photocurrents of less than 10 nA cm^{-2}. This indicates that the improvement in the Cu_2SnO_3 photocurrents upon the addition of CuO is not driven by CuO itself but rather the synergistic effect of the type-II band offset.

Comparison of the measured photocurrents for Cu_2SnO_3 and $Cu_{2-x}Li_xTiO_3$ to other Cu(I) oxides shows that these films are suitably large to warrant further investigation and optimization. For example, delafossite $CuRhO_2$ was developed to have a photocurrent of ∼1.0 mA cm^{-2} at −0.6 V versus SCE.[59] $CuFeO_2$ has achieved a similarly high photocurrent of ∼0.5 mA cm^{-2} at −0.6 V (SCE), albeit for CO_2 reduction rather than proton reduction.[60] Further examples of Cu(I)-based oxides and their cathodic photocurrents can be found in recent reports.[61] However, it should be noted that many of these reported photocurrents are under optimized conditions and/or consist of materials which have built upon years of prior research. Therefore, it should be emphasized that these photoelectrochemical data only represent an initial investigation of the potential of **I** and **II** as photocathodes. Follow-up investigations will be needed to develop the full potential of Cu_2SnO_3 and $Cu_{2-x}Li_xTiO_3$, such as by improving the film quality and preferential orientation of films along high carrier mobility directions, the addition of various dopants to improve carrier mobilities and conductivities, or systematic investigations of other surface co-catalysts and surface coatings to inhibit corrosion. These future research directions will not only serve to improve the Cu_2SnO_3 and $Cu_{2-x}Li_xTiO_3$ photocurrents but also continue to yield important fundamental insights in the field of photocatalysis.

CONCLUSIONS

The low-temperature synthesis of the first reported phases in the Cu−Sn−O and Cu−Ti−O systems were achieved using CuCl flux-based cation exchange reactions, yielding Cu_2SnO_3 (**I**) and $Cu_{2-x}Li_xTiO_3$ (**II**, $x_{min} \sim 0.4$). These compounds exhibit layered structures derived from the delafossite structure type. Their thermodynamic instability was found to be closely related to the occupation of octahedrally coordinated intralayer Cu(I) sites, which simultaneously lead to their much smaller band gaps of ∼2.31 eV for **I** and ∼1.46 eV for **II**. These hexagonal layers are bridged by other linearly coordinated Cu(I) cations, which are fully exchanged sites in both **I** and **II**. Both semiconductors were characterized by magnetic susceptibility measurements to confirm the +1 oxidation state of all copper cations. Total energy calculations reveal an increasing metastability with respect to decomposition to Cu_2O and SnO_2 or TiO_2 as a result of occupation of the intralayer sites by Cu(I) cations. In both semiconductors, their edge-shared hexagonal layers lead to highly dispersive conduction bands and small electron effective masses. Polycrystalline films also show clear evidence of their *p*-type behavior under irradiation in aqueous solutions. New fundamental relationships between the origin of metastability in Cu(I) oxide semiconductors, that is, octahedral coordination, and enhanced optical and photoelectrochemical properties have thus been revealed. The effectiveness of flux-mediated topotactic ion−exchange reactions in preparing metastable compounds has been demonstrated, and which can open the door to the future discovery of new metastable phases.

ASSOCIATED CONTENT

Supporting Information

The Supporting Information is available free of charge at https://pubs.acs.org/doi/10.1021/acs.chemmater.2c03563.

Additional results from refinements from the powder XRD data, SEM/EDS data for the particle morphologies and elemental concentrations, Tauc plots of UV−vis data, bulk phase analysis of the decomposition products with heating, and additional measurement results of photocurrents of polycrystalline films for both **I** and **II** (PDF)

AUTHOR INFORMATION

Corresponding Author

Paul A. Maggard − *Department of Chemistry, North Carolina State University, Raleigh, North Carolina 27695, United States;* orcid.org/0000-0002-3909-1590; Email: paul_maggard@ncsu.edu

Authors

Shaun O'Donnell − *Department of Chemistry, North Carolina State University, Raleigh, North Carolina 27695, United States*

Reinhard K. Kremer − *Max Planck Institute for Solid State Research, Stuttgart 70569, Germany;* orcid.org/0000-0001-9062-2361

Complete contact information is available at: https://pubs.acs.org/10.1021/acs.chemmater.2c03563

Notes

The authors declare no competing financial interest.

ACKNOWLEDGMENTS

The authors acknowledge primary support of this work from the National Science Foundation (DMR-2004455). Additional components of this research were performed in part at the Analytical Instrumentation Facility (AIF) at North Carolina State University, which is supported by the State of North Carolina and the National Science Foundation (Award ECCS-2025064). The AIF is a member of the North Carolina Research Triangle Nanotechnology Network (RTNN), a site in the National Nanotechnology Coordinated Infrastructure (NNCI).

REFERENCES

(1) Cheetham, A. K.; Seshadri, R.; Wudl, F. Chemical Synthesis and Materials Discovery. *Nat. Synth.* **2022**, *1*, 514−520.

(2) Mizushima, K.; Jones, P. C.; Wiseman, P. J.; Goodenough, J. B. Li_xCoO_2 (0<x<1): A New Cathode Material For Batteries of High Energy Density. *Mater. Res. Bull.* **1980**, *15*, 783−789.

(3) Johnston, W. D.; Heikes, R. R.; Sestrich, D. The Preparation, Crystallography, and Magnetic Properties of the $Li_xCo_{(1-x)}O$ System. *J. Phys. Chem. Solids* **1958**, *7*, 1−13.

(4) Brédas, J. L.; Buriak, J. M.; Caruso, F.; Choi, K. S.; Korgel, B. A.; Palacín, M. R.; Persson, K.; Reichmanis, E.; Schüth, F.; Seshadri, R.; et al. An Electrifying Choice for the 2019 Chemistry Nobel Prize: Goodenough, Whittingham, and Yoshino. *Chem. Mater.* **2019**, *31*, 8577−8581.

(5) Sun, W.; Holder, A.; Orvañanos, B.; Arca, E.; Zakutayev, A.; Lany, S.; Ceder, G. Thermodynamic Routes to Novel Metastable Nitrogen-Rich Nitrides. *Chem. Mater.* **2017**, *29*, 6936−6946.
(6) Sun, W.; Dacek, S. T.; Ong, S. P.; Hautier, G.; Jain, A.; Richards, W. D.; Gamst, A. C.; Persson, K. A.; Ceder, G.The Thermodynamic Scale of Inorganic Crystalline Metastability. *Sci. Adv.***2016**, *2*(). DOI: 10.1126/sciadv.1600225
(7) Aykol, M.; Dwaraknath, S. S.; Sun, W.; Persson, K. A. Thermodynamic Limit for Synthesis of Metastable Inorganic Materials. *Sci. Adv.* **2018**, *4*, 1−8.
(8) Pöhls, J. H.; Heyberger, M.; Mar, A. Comparison of Computational and Experimental Inorganic Crystal Structures. *J. Solid State Chem.* **2020**, *290*, 121557.
(9) O'Donnell, S.; Chung, C.-C.; Carbone, A.; Broughton, R.; Jones, J. L.; Maggard, P. A. Pushing the Limits of Metastability in Semiconducting Perovskite Oxides for Visible-Light-Driven Water Oxidation. *Chem. Mater.* **2020**, *32*, 3054−3064.
(10) O'Donnell, S.; Smith, A.; Carbone, A.; Maggard, P. A. Structure, Stability, and Photocatalytic Activity of a Layered Perovskite Niobate after Flux-Mediated Sn(II) Exchange. *Inorg. Chem.* **2022**, *61*, 4062−4070.
(11) Gabilondo, E. A.; O'Donnell, S.; Broughton, R.; Jones, J. L.; Maggard, P. A. Synthesis and Stability of Sn(II)-Containing Perovskites: $(Ba,Sn^{II})Hf^{IV}O_3$ versus $(Ba,Sn^{II})Sn^{IV}O_3$. *J. Solid State Chem.* **2021**, *2021*, 302.
(12) Martinolich, A. J.; Kurzman, J. A.; Neilson, J. R. Circumventing Diffusion in Kinetically Controlled Solid-State Metathesis Reactions. *J. Am. Chem. Soc.* **2016**, *138*, 11031−11037.
(13) Chamorro, J. R.; McQueen, T. M. Progress toward Solid State Synthesis by Design. *Acc. Chem. Res.* **2018**, *51*, 2918−2925.
(14) O'Donnell, S.; Hamilton, A.; Maggard, P. A. Fast Flux Reaction Approach for the Preparation of Sn_2TiO_4: Tuning Particle Sizes and Photocatalytic Properties. *J. Electrochem. Soc.* **2019**, *166*, H3084−H3090.
(15) Cushing, B. L.; Wiley, J. B. Topotactic Routes to Layered Calcium Cobalt Oxides. *J. Solid State Chem.* **1998**, *141*, 385−391.
(16) Chondroudis, K.; Kanatzidis, M. C. New Topotactic Derivatives of the Open-Framework Semiconductor KBi_3S_5 via a Low-Temperature Solid-State Ion-Exchange Route. *J. Solid State Chem.* **1998**, *136*, 328−332.
(17) Toby, B. H.; Von Dreele, R. B. GSAS-II: The Genesis of a Modern Open-Source All Purpose Crystallography Software Package. *J. Appl. Crystallogr.* **2013**, *46*, 544−549.
(18) Simmons, E. L. Reflectance Spectroscopy: Application of the Kubelka-Munk Theory to the Rates of Photoprocesses of Powders. *Appl. Opt.* **1976**, *15*, 951.
(19) Kresse, G.; Furthmüller, J. Efficiency of Ab-Initio Total Energy Calculations for Metals and Semiconductors Using a Plane-Wave Basis Set. *Comput. Mater. Sci.* **1996**, *6*, 15−50.
(20) Perdew, J. .; Burke, L.; Ernzerhof, M. Generalized Gradient Approximation Made Simple. *Phys. Rev. Lett.* **1996**, *77*, 3865.
(21) M Ganose, A.; J Jackson, A.; O Scanlon, D. Sumo: Command-Line Tools for Plotting and Analysis of Periodic Ab Initio Calculations. *J. Open Source Softw.* **2018**, *3*, 717.
(22) Hautier, G.; Ong, S. P.; Jain, A.; Moore, C. J.; Ceder, G. Accuracy of Density Functional Theory in Predicting Formation Energies of Ternary Oxides from Binary Oxides and Its Implication on Phase Stability. *Phys. Rev. B - Condens. Matter Mater. Phys.* **2012**, *85*, 155208.
(23) Emery, A. A.; Wolverton, C. High-Throughput DFT Calculations of Formation Energy, Stability and Oxygen Vacancy Formation Energy of ABO_3 Perovskites. *Sci. Data* **2017**, *4*, 1−10.
(24) Saal, J. E.; Kirklin, S.; Aykol, M.; Meredig, B.; Wolverton, C. Materials Design and Discovery with High-Throughput Density Functional Theory: The Open Quantum Materials Database (OQMD). *Jom* **2013**, *65*, 1501−1509.
(25) Kirklin, S.; Saal, J. E.; Meredig, B.; Thompson, A.; Doak, J. W.; Aykol, M.; Rühl, S.; Wolverton, C. The Open Quantum Materials Database (OQMD): Assessing the Accuracy of DFT Formation Energies. *npj Comput. Mater.* **2015**, *1*, 15010.
(26) Gillan, E. G.; Kaner, R. B. Rapid, Energetic Metathesis Routes to Crystalline Metastable Phases of Zirconium and Hafnium Dioxide. *J. Mater. Chem.* **2001**, *11*, 1951−1956.
(27) Rognerud, E. G.; Rom, C. L.; Todd, P. K.; Singstock, N. R.; Bartel, C. J.; Holder, A. M.; Neilson, J. R. Kinetically Controlled Low-Temperature Solid-State Metathesis of Manganese Nitride Mn_3N_2. *Chem. Mater.* **2019**, *31*, 7248−7254.
(28) Todd, P. K.; Neilson, J. R. Selective Formation of Yttrium Manganese Oxides through Kinetically Competent Assisted Metathesis Reactions. *J. Am. Chem. Soc.* **2019**, *141*, 1191−1195.
(29) Abramchuk, M.; Ozsoy-Keskinbora, C.; Krizan, J. W.; Metz, K. R.; Bell, D. C.; Tafti, F. Cu_2IrO_3: A New Magnetically Frustrated Honeycomb Iridate. *J. Am. Chem. Soc.* **2017**, *139*, 15371−15376.
(30) Abramchuk, M.; Lebedev, O. I.; Hellman, O.; Bahrami, F.; Mordvinova, N. E.; Krizan, J. W.; Metz, K. R.; Broido, D.; Tafti, F. Crystal Chemistry and Phonon Heat Capacity in Quaternary Honeycomb Delafossites: $Cu[Li_{1/3}Sn_{2/3}]O_2$ and $Cu[Na_{1/3}Sn_{2/3}]O_2$. *Inorg. Chem.* **2018**, *57*, 12709−12717.
(31) Owen, M. Magnetochemische Untersuchungen. Die Thermomagnetischen Eigenschaften Der Elemente. *Ann. Phys.* **1912**, *342*, 657−699.
(32) Honda, K. Susceptibility of the Elements. *Ann. Phys.* **1910**, *337*, 1027−1063.
(33) Bain, G. A.; Berry, J. F. Diamagnetic Corrections and Pascal's Constants. *J. Chem. Educ.* **2008**, *85*, 532−536.
(34) Hiraga, H.; Makino, T.; Fukumura, T.; Weng, H.; Kawasaki, M. Electronic Structure of the Delafossite-Type $CuMO_2$ (M=Sc, Cr, Mn, Fe, and Co): Optical Absorption Measurements and First-Principles Calculations. *Phys. Rev. B - Condens. Matter Mater. Phys.* **2011**, *84*, 2−5.
(35) Kandpal, H. C.; Seshadri, R. First-Principles Electronic Structure of the Delafossites ABO_2 (A=Cu, Ag, Au; B = Al, Ga, Sc, In, Y): Evolution of D10-D10 Interactions. *Solid State Sci.* **2002**, *4*, 1045−1052.
(36) Mizoguchi, H.; Eng, H. W.; Woodward, P. M. Probing the Electronic Structures of Ternary Perovskite and Pyrochlore Oxides Containing Sn^{4+} or Sb^{5+}. *Inorg. Chem.* **2004**, *43*, 1667−1680.
(37) Mizoguchi, H.; Woodward, P. M. Electronic Structure Studies of Main Group Oxides Possessing Edge-Sharing Octahedra: Implications for the Design of Transparent Conducting Oxides. *Chem. Mater.* **2004**, *16*, 5233−5248.
(38) Perdew, J. P. Density Functional Theory and the Band Gap Problem. *Int. J. Quantum Chem.* **1985**, *28*, 497−523.
(39) Borges, P. D.; Scolfaro, L. M. R.; Alves, H. W. L.; da Silva, E. F. DFT Study of the Electronic, Vibrational, and Optical Properties of SnO_2. *Theor. Chem. Acc.* **2010**, *126*, 39−44.
(40) Moreira, E.; Henriques, J. M.; Azevedo, D. L.; Caetano, E. W. S.; Freire, V. N.; Albuquerque, E. L. Structural and Electronic Properties of $Sr_xBa_{1-x}SnO_3$ from First Principles Calculations. *J. Solid State Chem.* **2012**, *187*, 186−194.
(41) Jiang, C. M.; Reyes-Lillo, S. E.; Liang, Y.; Liu, Y. S.; Liu, G.; Toma, F. M.; Prendergast, D.; Sharp, I. D.; Cooper, J. K. Electronic Structure and Performance Bottlenecks of $CuFeO_2$ Photocathodes. *Chem. Mater.* **2019**, *31*, 2524−2534.
(42) Hautier, G.; Miglio, A.; Ceder, G.; Rignanese, G. M.; Gonze, X. Identification and Design Principles of Low Hole Effective Mass p-Type Transparent Conducting Oxides. *Nat. Commun.* **2013**, *4*, 1−7.
(43) Moreira, M.; Afonso, J.; Crepelliere, J.; Lenoble, D.; Lunca-Popa, P. A Review on the p-Type Transparent Cu−Cr−O Delafossite Materials. *J. Mater. Sci.* **2022**, *57*, 3114−3142.
(44) Nie, X.; Wei, S. H.; Zhang, S. B. Bipolar Doping and Band-Gap Anomalies in Delafossite Transparent Conductive Oxides. *Phys. Rev. Lett.* **2002**, *88*, 4.
(45) Joshi, U. A.; Maggard, P. A. $CuNb_3O_8$: A p-Type Semiconducting Metal Oxide Photoelectrode. *J. Phys. Chem. Lett.* **2012**, *3*, 1577−1581.

(46) Boltersdorf, J.; Sullivan, I.; Shelton, T. L.; Wu, Z.; Gray, M.; Zoellner, B.; Osterloh, F. E.; Maggard, P. A. Flux Synthesis, Optical and Photocatalytic Properties of n-Type Sn_2TiO_4: Hydrogen and Oxygen Evolution under Visible Light. *Chem. Mater.* **2016**, *28*, 8876−8889.
(47) Rajeshwar, K.; Hossain, M. K.; Macaluso, R. T.; Janáky, C.; Varga, A.; Kulesza, P. J. Review—Copper Oxide-Based Ternary and Quaternary Oxides: Where Solid-State Chemistry Meets Photoelectrochemistry. *J. Electrochem. Soc.* **2018**, *165*, H3192−H3206.
(48) Zoellner, B.; O'Donnell, S.; Wu, Z.; Itanze, D.; Carbone, A.; Osterloh, F. E.; Geyer, S.; Maggard, P. A. Impact of Nb(V) Substitution on the Structure and Optical and Photoelectrochemical Properties of the $Cu_5(Ta_{1-x}Nb_x)_{11}O_{30}$ Solid Solution. *Inorg. Chem.* **2019**, *58*, 6845−6857.
(49) Joshi, U. A.; Palasyuk, A. M.; Maggard, P. A. Photoelectrochemical Investigation and Electronic Structure of p-Type $CuNbO_3$ Photocathode. *J. Phys. Chem. C* **2011**, *115*, 13534−13539.
(50) Sahoo, P. P.; Zoellner, B.; Maggard, P. A. Optical, Electronic, and Photoelectrochemical Properties of the p-Type $Cu_{3-x}VO_4$ Semiconductor. *J. Mater. Chem. A* **2015**, *3*, 4501−4509.
(51) Hossain, M. K.; Samu, G. F.; Gandha, K.; Santhanagopalan, S.; Liu, J. P.; Janáky, C.; Rajeshwar, K. Solution Combustion Synthesis, Characterization, and Photocatalytic Activity of $CuBi_2O_4$ and Its Nanocomposites with CuO and α-Bi_2O_3. *J. Phys. Chem. C* **2017**, *121*, 8252−8261.
(52) Somasundaram, S.; Ramannairchenthamarakshan, C.; Detacconi, N. R.; Rajeshwar, K. Photocatalytic Production of Hydrogen from Electrodeposited p-Cu_2O Film and Sacrificial Electron Donors. *Int. J. Hydrogen Energy* **2007**, *32*, 4661−4669.
(53) Zoellner, B.; Stuart, S.; Chung, C. C.; Dougherty, D. B.; Jones, J. L.; Maggard, P. A. $CuNb_{1-x}Ta_xO_3$ ($x \leq 0.25$) Solid Solutions: Impact of Ta(V) Substitution and Cu(I) Deficiency on Their Structure, Photocatalytic, and Photoelectrochemical Properties. *J. Mater. Chem. A* **2016**, *4*, 3115−3126.
(54) Won, D. H.; Choi, C. H.; Chung, J.; Woo, S. I. Photoelectrochemical Production of Formic Acid and Methanol from Carbon Dioxide on Metal-Decorated CuO/Cu_2O-Layered Thin Films under Visible Light Irradiation. *Appl. Catal. B Environ.* **2014**, *158-159*, 217−223.
(55) Firouzan, F.; Vali, A.; Rajeshwar, K. Editors' Choice—Perspective—Bipolar Photoactivity: The Anomalous Case of Electrodeposited Copper Oxide Films. *J. Electrochem. Soc.* **2020**, *167*, 136505.
(56) Sullivan, I.; Sahoo, P. P.; Fuoco, L.; Hewitt, A. S.; Stuart, S.; Dougherty, D.; Maggard, P. A. Cu-Deficiency in the p-Type Semiconductor $Cu_{5-x}Ta_{11}O_{30}$: Impact on Its Crystalline Structure, Surfaces, and Photoelectrochemical Properties. *Chem. Mater.* **2014**, *26*, 6711−6721.
(57) King, N.; Sahoo, P. P.; Fuoco, L.; Stuart, S.; Dougherty, D.; Liu, Y.; Maggard, P. A. Copper Deficiency in the p-Type Semiconductor $Cu_{1-x}Nb_3O_8$. *Chem. Mater.* **2014**, *26*, 2095−2104.
(58) Sohag, Z.; O'Donnell, S.; Fuoco, L.; Maggard, P. A. A Metastable p-Type Semiconductor as a Defect-Tolerant Photoelectrode. *Molecules* **2021**, *26*, 6830.
(59) Gu, J.; Yan, Y.; Krizan, J. W.; Gibson, Q. D.; Detweiler, Z. M.; Cava, R. J.; Bocarsly, A. B. p-Type $CuRhO_2$ as a Self-Healing Photoelectrode for Water Reduction under Visible Light. *J. Am. Chem. Soc.* **2014**, *136*, 830−833.
(60) Gu, J.; Wuttig, A.; Krizan, J. W.; Hu, Y.; Detweiler, Z. M.; Cava, R. J.; Bocarsly, A. B. Mg-Doped $CuFeO_2$ Photocathodes for Photoelectrochemical Reduction of Carbon Dioxide. *J. Phys. Chem. C* **2013**, *117*, 12415−12422.
(61) Sullivan, I.; Zoellner, B.; Maggard, P. A. Copper(I)-Based p-Type Oxides for Photoelectrochemical and Photovoltaic Solar Energy Conversion. *Chem. Mater.* **2016**, *28*, 5999−6016.

Recommended by ACS

Influence of Ion Exchange on Photoresponsive Properties of Potassium Poly(heptazine imide)
Mai Hattori, Kaname Kanai, *et al.*
JANUARY 26, 2023
CHEMISTRY OF MATERIALS
READ

Data-Driven Design of Classes of Ruthenium Nanoparticles Using Multitarget Bayesian Inference
Jonathan Y. C. Ting, Amanda S. Barnard, *et al.*
JANUARY 09, 2023
CHEMISTRY OF MATERIALS
READ

Phase Competition and Strong SHG Responses of the $Li_2M^{II}M^{IV}Se_4$ Family: Atom Response Theory Predictions versus Experimental Results
Wen-Dong Yao, Shuiquan Deng, *et al.*
JANUARY 24, 2023
CHEMISTRY OF MATERIALS
READ

Designing CuO–SiO_2 and Cu^0–SiO_2 Monolithic Ceramics Bearing Hierarchical Porosity Toward Robust and Cycling CO Oxidation Properties
Antoine Vardon, Rénal Backov, *et al.*
DECEMBER 22, 2022
CHEMISTRY OF MATERIALS
READ

Get More Suggestions >

https://doi.org/10.1021/acs.chemmater.2c03563
Chem. Mater. 2023, 35, 1404−1416